Advanced Powder Technology 36 (2025) 105055

Contents lists available at ScienceDirect

Advanced Powder Technology

journal homepage: www.elsevier.com/locate/apt

Fabrication and magnetic properties of iron-based nano-crystalline alloys with high magnetic induction

Han Gao [a,1], Yanan Chen [a,1], Bo Lin [a], Yuanfei Cai [a], Xiaoying Huang [a], Meng Gao [a,b], Yaocen Wang [c], Likun Chen [d], Wei Xu [a], Xing Tong [e], Hai Guo [f], Wenbo Wang [g], Mingliang Xiang [a,*], Jun-Qiang Wang [a,b,*], Yan Zhang [a,b,*]

[a] CAS Key Laboratory of Magnetic Materials and Devices, and Zhejiang Province Key Laboratory of Magnetic Materials and Application Technology, Ningbo Institute of Materials Technology and Engineering, Chinese Academy of Science, Ningbo 315201, China
[b] Center of Materials Science and Optoelectronics Engineering, University of Chinese Academy of Sciences, Beijing 100049, China
[c] School of Physical Science and Technology, Northwestern Polytechnical University, Xi'an 710072, China
[d] Institute for Materials Research, Tohoku University, Sendai 980-8577, Japan
[e] Songshan Lake Materials Laboratory, Dongguan 523808, China
[f] Shenzhen Sunlord Electronics Co., Ltd., Shenzhen 518110, China
[g] Yongjiang Laboratory, Ningbo 315202, China

ARTICLE INFO

Article history:
Received 28 February 2025
Received in revised form 18 August 2025
Accepted 1 September 2025

Keywords:
Saturated magnetic induction
Soft magnetic
Gas atomization
Amorphous
Nano-crystalline

ABSTRACT

Fe-Si-B-P-Cu-C amorphous alloys with high amorphous forming ability and saturation magnetic induction were developed by optimizing B and P concentrations alongside Ni doping. Gas-atomized $Fe_{80.5}Si_{0.5}B_{10.5}P_5Cu_{0.5}C_2Ni_1$ powders exhibited full amorphous structure, achieving a high saturation magnetic induction of 180 emu/g after annealing at 420 °C. The annealed powders demonstrated excellent soft magnetic properties, including high permeability and low core loss. Phosphoric acid passivation further reduced core loss by 26 % while retaining a high saturation magnetic induction of 176.8 emu/g. These properties make the alloy a promising candidate for high-power-density and miniaturized magnetic applications.

1. Introduction

The rapid advancement of power electronics toward miniaturization, high-frequency operation, and energy efficiency has intensified the demand for high-performance soft magnetic materials [1,2]. Fe-based amorphous and nanocrystalline alloys outperform traditional silicon steel due to their superior saturation magnetic induction (B_s), permeability (μ_e), low coercivity (H_c), and reduced core loss (P_{cv}) [3,4], making them ideal for high-frequency applications such as transformers, inductors, and switching power supplies [5–7]. Among these properties, B_s is particularly critical for enhancing power density in compact devices [8–10].

While nanocrystalline structures obtained through annealing amorphous precursors can achieve high B_s [11], the prerequisite is sufficient amorphous-forming ability (AFA), which is highly sensitive to composition, especially Fe content [7,12]. Although high Fe concentrations improve B_s, they often compromise AFA [13,14]. Industrial production of amorphous powders relies on mechanical crushing or atomization [15–18]. Gas-atomized powders, with their spherical morphology and smooth surfaces, offer advantages over irregular crushed powders, minimizing eddy current losses [17,19]. which is beneficial for the magnetic stability of the powder at high frequency. However, gas atomization requires alloys with high AFA, necessitating careful compositional design.

Metalloid elements (Si, B, P) enhance AFA but reduce B_s at lower Fe concentrations [20–24]. NANOMET materials exhibit high B_s, but their high heating ramp rates during heat treatment limit their industrial applications [1,8,25]. Previous studies have shown that

* Corresponding authors at: CAS Key Laboratory of Magnetic Materials and Devices, and Zhejiang Province Key Laboratory of Magnetic Materials and Application Technology, Ningbo Institute of Materials Technology and Engineering, Chinese Academy of Science, Ningbo 315201, China.

E-mail addresses: xiangmingliang@nimte.ac.cn (M. Xiang), jqwang@nimte.ac.cn (J.-Q. Wang), yzhang@nimte.ac.cn (Y. Zhang).

[1] These authors contribute equally to this work.

https://doi.org/10.1016/j.apt.2025.105055

doping with C element enables the formation of fine and uniform nanocrystalline structures through slow heat treatment, leading to grain refinement and reduced the H_c [26]. Similarly, Ni doping has been reported to enhance AFA while refining α-(Fe,Ni) grains, resulting in higher B_s and lower H_c [27]. Additionally, a uniform insulating layer coating the powder particles can isolate particle-to-particle contact within the powder core, effectively reducing eddy current loss and enhancing the overall efficiency of the device [28–31]. Recent studies demonstrated that phosphoric acid passivation is an effective method to suppress eddy current losses [32].

To achieve high B_s in Fe-based nanocrystalline powders with excellent soft magnetic properties, this study focused on the fabrication of amorphous/nanocrystalline alloys by doping Ni into Fe-Si-B-P-Cu-C and varying the ratios of B and P. The annealing process was employed to control and optimize the structure. The AFA, thermal stability, crystallization behavior, microstructure, and soft magnetic properties of both ribbon and powder samples were systematically investigated and analyzed. This study significantly enhances the AFA while maintaining high B_s. This approach offers a unique pathway to balance the trade-off between high AFA and high magnetic performance, addressing key challenges in the design of gas-atomized soft magnetic powders.

2. Experiments

Master alloys with a nominal composition of $Fe_{81.5-x}Si_{0.5}B_{4.5}P_{11}Cu_{0.5}C_2Ni_x$ (x = 0, 1, 2, and 4 at.%) and $Fe_{80.5}Si_{0.5}B_{4.5+x}P_{11-x}Cu_{0.5}C_2Ni_1$ (x = 0, 2, 4, and 6 at.%) were prepared by high frequency induction melting of a mixture of high-purity raw material (99.99 mass.% Fe, 99.99 mass.% Ni, 99.99 mass.% Si, 99.98 mass.% B, 99.99 mass.% Cu, and 99.99 mass.% C, 99.9 mass.% pre-melted Fe_5P_3) under a pure Ar atmosphere. Each of the master alloys was repeatedly melted three times to ensure uniformity. Thin ribbons of $Fe_{81.5-x}Si_{0.5}B_{4.5}P_{11}Cu_{0.5}C_2Ni_x$ in the quenched state with a width of 1–2 mm and a thickness of 20 μm were prepared by melt spinning in air. The powders of $Fe_{80.5}Si_{0.5}B_{4.5+x}P_{11-x}Cu_{0.5}C_2Ni_1$ were prepared by gas atomization under a pure Ar atmosphere, and the powders were highly spherical with an average particle size of 17 μm.

The phosphoric acid with different concentrations (0.5, 1, 1.5, 2, and 4 wt.%) were poured into alcohol to dissolve the preparation of phosphoric acid solution, and then $Fe_{80.5}Si_{0.5}B_{10.5}P_5Cu_{0.5}C_2Ni_1$ powders were poured into phosphoric acid solution, and stirred under ultrasonic stirring for 30 min passivation. Epoxy resin (2 % of the mass of the magnetic powder) was mixed with the powder particles for electrical insulation. The mixed powders were dried in an oven. The toroidal cores with the outer and inner diameters of 13 and 8 mm, were obtained by the cold pressing method at a pressure of 1.8 GPa. Finally, the powder cores were annealed under vacuum (≤5×10^{-3} Pa) in a quartz tube at a temperature of 400–500 °C for 60 min.

The physical phases of ribbon, powder, and powder core samples were analyzed by X-ray diffraction (XRD, D8 DISCOVER) with Cu Ka radiation and a transmission electron microscopy (TEM, Talos F200x). Thermal properties were studied by using a differential scanning calorimetry (DSC, NETZSCH 404C) at a heating rate of 40 °C/min under flowing Ar gas. Hysteresis loops of the powder and ribbon samples were measured by a vibrating sample magnetometer (VSM, Lakeshore 7410) and a DC B-H loop tracer (Rikken Denshi BHS-40S) with a solenoidal coil under a maximum applied field of 1 T (800 kA/m) and 800 A/m, respectively. Here, the saturation magnetization (M_s) was obtained from VSM data and the saturated magnetic flux density ($B_s \approx \mu_0 M_s$) was calculated from M_s. The μ_e of the toroidal samples was measured with an impedance analyzer (Agilent 4294A) in the frequency range of 1 kHz to 110 MHz. The measurements of P_{cv} were performed by using an AC B-H analyzer (IWATSU SY-8218). The surface morphology of the powders was observed by a scanning electron microscopy (SEM, ZEISS EVO 18). The present work was used to study the molecular structure by NICCOLET Model 6700 Intelligent Fourier Infrared Spectrometer (FTIR). Density (ρ) of the cores was estimated by weight and physical volume of the toroidal samples.

3. Results and discussion

3.1. Compositional design of high AFA alloy with high iron concentration

The $Fe_{81.5}Si_{0.5}B_{4.5}P_{11}Cu_{0.5}C_2$ alloy was doped with Ni elements to explore its effect on the AFA. Fig. 1(a) shows the XRD pattern of the ribbon free surfaces for the $Fe_{81.5-x}Si_{0.5}B_{4.5}P_{11}Cu_{0.5}C_2Ni_x$ (x = 0, 1, 2, and 4 at.%) alloys after quenching. It can be seen that with the addition of Ni, a distinct halo peak o appears at 2θ = 45°, with no sharp diffraction peaks detected, confirming the amorphous structure of the ribbons. Moreover, as the Ni concentration increases, the halo peaks become progressively flatter, indicating that Ni addition enhances the amorphous-forming ability of the alloy. The DSC curves of $Fe_{81.5-x}Si_{0.5}B_{4.5}P_{11}Cu_{0.5}C_2Ni_x$ (x = 0, 1, 2, and 4 at.%) soft magnetic alloy ribbons are shown in Fig. 1(b). All curves exhibit two exothermic peaks, indicating that different compositions underwent two stages of crystallization, corresponding to the precipitation of α-Fe and iron boride phases, respectively. As the Ni concentration increases, the first on-set crystallization temperature (T_{x1}) gradually shifts to higher temperatures, demonstrating that the addition of Ni enhances the AFA and promotes the thermal stability of the alloy. When the Ni concentration reaches 2 at.%, the second on-set crystallization temperature (T_{x2}) also shifts to the higher temperatures, but then shifts back to lower temperatures with further increases in Ni concentration. This suggests that adding an appropriate amount of Ni can inhibit the formation of secondary phases such as Fe-B. Although the temperature difference ΔT ($\Delta T = T_{x2} - T_{x1}$) between T_{x2} and T_{x1} decreased slightly, it remains around 70 °C . This indicates that the precipitation and growth of single α-Fe grains can be controlled by adjusting the temperature and time, while maintaining a wide heat treatment window, which is beneficial for selecting the appropriate annealing temperature and duration.

The H_c changes of the ribbons after annealing at 350460 °C for 30 min are shown in Fig. 2(a). The H_c of each alloy composition exhibits a "W"-type trend as the annealing temperature increases. According to Herzer's formula [33,34], the average grain size (D) of α-Fe crystals is proportional to H_c, and H_c follows a D^3-power law when H_c < 20 A/m. When the annealing temperature (T_a) is 420 °C, H_c decreases sharply due to the gradual precipitation of small and dense α-Fe grains. As T_a increases further, the α-Fe grain size grows and iron boride phases begin to precipitate. The magnetic coupling between the nanocrystalline and amorphous phases weakens, and the presence of pinning sites makes it more difficult for the magnetic domain walls to move, thus hindering the magnetization process. This results in a sharp increase in H_c. As shown in Fig. 2(b), the trends of H_c and D for each composition of ribbon alloys are consistent after annealing at 420 °C for 30 min. When x = 1, the grain size is 14.8 nm, and the H_c reaches its lowest value of 3.7 A/m. In addition, with the small adddition of Ni, the B_s of the alloy ribbons is also significantly improved. For Fe-based amorphous alloys, a larger the magnetic moment corresponds to a higher B_s [35]. According to the experimental results from previous studies [27,36,37], the B_s of the alloys decreases significantly with the addition of Ni when it substitutes a large proportion of Fe elements (≥10 at.%). However, the Ni atoms themselves have a certain degree of ferro-

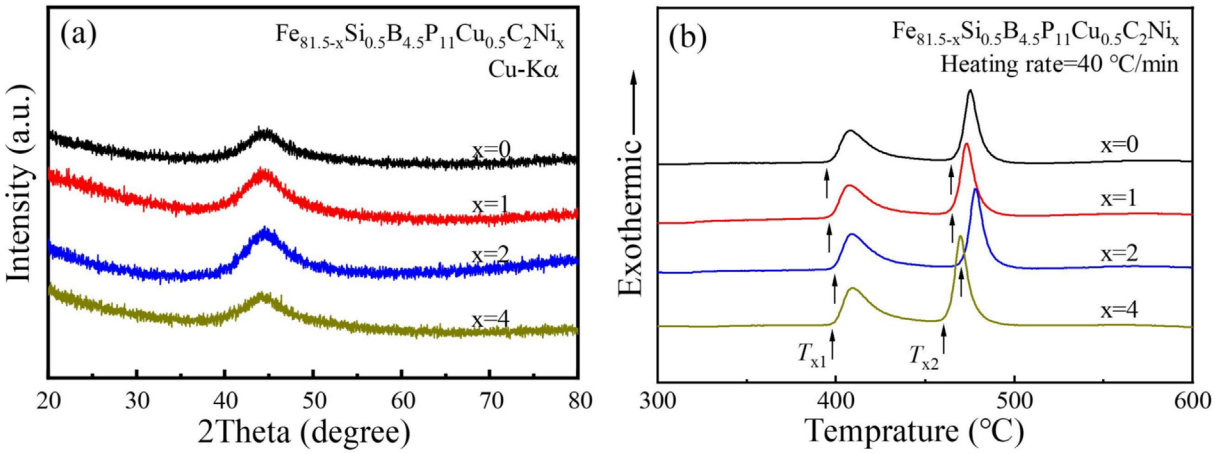

Fig. 1. (a) XRD patterns and (b) DSC curves of $Fe_{81.5-x}Si_{0.5}B_{4.5}P_{11}Cu_{0.5}C_2Ni_x$ (x = 0, 1, 2, and 4 at.%) alloy ribbons.

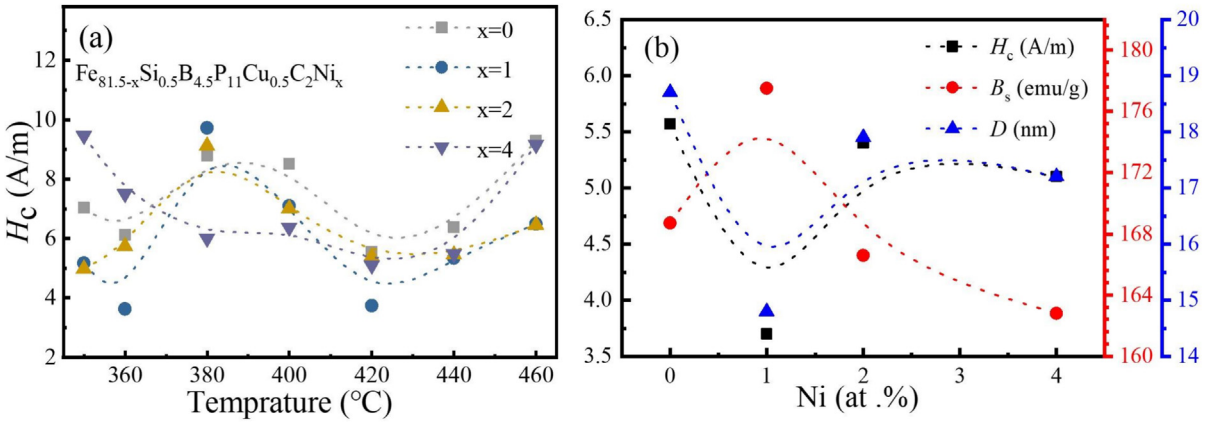

Fig. 2. (a) H_c at different T_a and (b) H_c, B_s, and D after heat treatment at 420 ℃ of $Fe_{81.5-x}Si_{0.5}B_{4.5}P_{11}Cu_{0.5}C_2Ni_x$ (x = 0, 1, 2, and 4 at.%) ribbons.

magnetism and the results were found to be different in this experiment. When the Ni concentration is 1 at.%, the B_s increases and stabilizes at a favorable value of 177.5 emu/g. This indicates that B_s can be maintained without an increase in H_c by adding a small amount of Ni (1 at.%), which aligns with previous studies on the topic [38]. As the Ni concentration increases to 4 at.%, B_s rapidly decreases to 162.8 emu/g, due to the smaller magnetic moment of Ni compared to Fe.

3.2. Compositional design with high AFA and high B_s on soft magnetic powder

Based on previous experiments on alloy ribbons, it was found that the addition of appropriate amount of Ni enhanced the AFA and thermal stability of the alloy. After crystallization annealing, the ribbons exhibited the best soft magnetic properties when the Ni concentration was 1 at.%. In order to obtain soft magnetic powders with high AFA and B_s, the concentrations of B and P elements were further adjusted on the basis of $Fe_{80.5}Si_{0.5}B_{4.5+x}P_{11-x}Cu_{0.5}C_2Ni_1$ alloy composition.

Fig. 3(a) shows the XRD patterns of gas-atomized $Fe_{80.5}Si_{0.5}B_{4.5+x}P_{11-x}Cu_{0.5}C_2Ni_1$ (x = 0, 2, 4, 6 at.%) powders. It can be observed that for x values of 4–6 at.%, only a broad amorphous halo peak is present near 2θ = 45°, indicating an amorphous structure. However, for x values of 0–2 at.%, α-Fe and a slight crystallization peak corresponding to Fe-B appear in the pattern, suggesting partial crystallization. This indicates that partial substitution of B for P improves the AFA of the powders. The smaller atomic radius of B compared to P increases the atomic size difference between atoms when P is replaced by B. The addition of smaller atoms helps promote the formation of a more compact stacking structure, which reduces the long-range diffusion of atoms, thereby enhancing the AFA. The DSC curves of $Fe_{80.5}Si_{0.5}B_{4.5+x}P_{11-x}Cu_{0.5}C_2Ni_1$ (x = 0, 2, 4, 6 at.%) powders are shown in Fig. 3(b). For the samples with x = 4 at.% and x = 6 at.%, two exothermic peaks are observed, corresponding to the precipitation of the α-Fe and Fe-B phases, respectively. For the samples with x = 4 at.% and x = 6 at.%, two exothermic peaks are observed, corresponding to the precipitation of the α-Fe and Fe-B phases, respectively. Additionally, it is observed that as the B concentration increases, ΔT gradually increases, thereby broadening the annealing window. When x = 6 at.%, ΔT reaches 80 °C. Furthermore, as the B concentration increases, T_{x1} shifts to higher temperatures, promoting the formation of the amorphous phase and enhancing the AFA. Simultaneously, T_{x2} also shifts to the right, inhibiting the formation of the second phase.

To investigate the effect of B and P elemental concentrations on the magnetic properties, the hysteresis loops curves of $Fe_{80.5}Si_{0.5}B_{4.5+x}P_{11-x}Cu_{0.5}C_2Ni_1$ (x = 0, 2, 4, and 6 at.%) powders are shown in Fig. 4. The B_s of powder was positively correlated with the increase of B concentration, with B_s rising from 162.9 to 171.5 emu/g, reaching a maximum value at x = 6. The improvement of B_s can be explained from the following aspects. The B_s of amorphous alloys is related to the average magnetic moment of

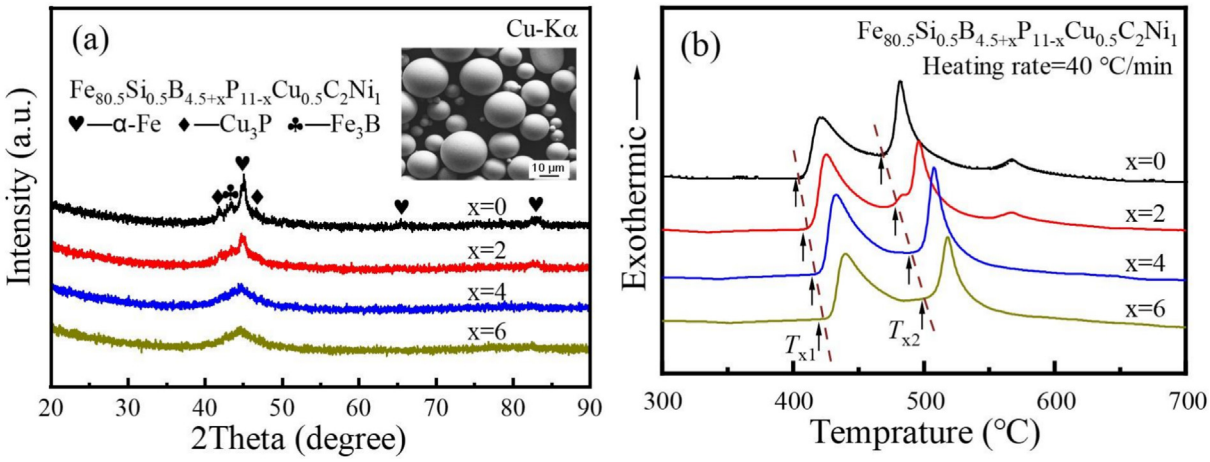

Fig. 3. (a) XRD patterns (The inset diagram is SEM image of powders) and (b) DSC curves of gas-atomized $Fe_{80.5}Si_{0.5}B_{4.5+x}P_{11-x}Cu_{0.5}C_2Ni_1$ (x = 0, 2, 4, 6 at.%) powders.

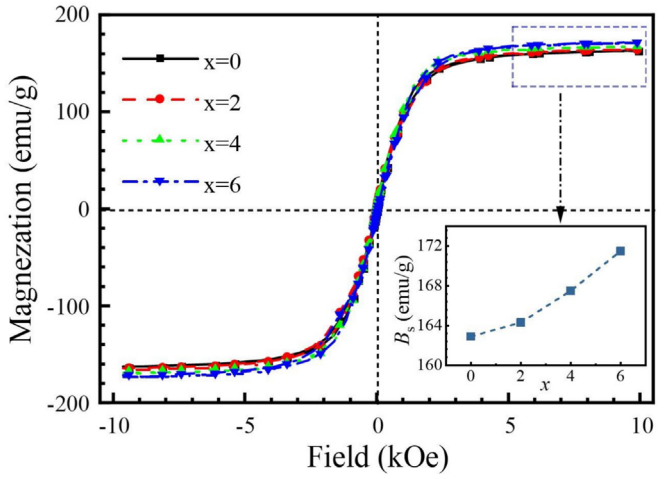

Fig. 4. Hysteresis loops of $Fe_{80.5}Si_{0.5}B_{4.5+x}P_{11-x}Cu_{0.5}C_2Ni_1$ (x = 0, 2, 4, and 6 at.%) powders (The inset picture shows B_s of powders with different composition).

the alloy, and a larger the magnetic results in higher B_s. In transition metals, the electrons in the d orbitals can be easily transferred from the region not involved in hybridization to the region involved in p-d hybridization bonding. The migration of electrons from the d energy band of the transition element to the region involved in p-d hybridization results in the formation of less easily polarizable p-d hetero-bonds, and at the same time this migration of electrons reduces the magnetic moment of the alloy [39]. Electrons in the d band of transition metals are more likely to form hybrid p-d bonds with the outermost electrons of the P element. Therefore, Therefore, replacing P with B inhibits the formation of p-d bonds, leading to an increase in B_s.

Combined with the results of XRD, DSC and VSM, gas-atomized $Fe_{80.5}Si_{0.5}B_{10.5}P_5Cu_{0.5}C_2Ni_1$ powders have a high AFA, a wide T_a window (ΔT = 80 °C) and the best comprehensive magnetic properties ($B_s \approx 171.5$ emu/g). Follow-up work is therefore carried out by this component.

3.3. Magnetic softness of $Fe_{80.5}Si_{0.5}B_{10.5}P_5Cu_{0.5}C_2Ni_1$ nano-crystalline powders

To study the magnetic properties of nano-crystalline powders, the effect of T_a on the microstructure and magnetic properties of $Fe_{80.5}Si_{0.5}B_{9.5}P_5Cu_{0.5}C_2Ni_1$ amorphous powders were investigated. Fig. 5(a) shows the XRD patterns of $Fe_{80.5}Si_{0.5}B_{9.5}P_5Cu_{0.5}C_2Ni_1$ powders annealed at different temperatures for 60 min. When the T_a is 400 °C, the crystallization peak begins to appear, and the crystallization strength increases gradually with the increase of the annealing temperature. The powder exhibits three peaks corresponding to α-Fe at 400 and 420 °C. When the annealing temperature rises to 440 °C, the precipitation of Fe-B phase starts to appear in the powders. Fig. 5(b) shows the corresponding DSC curves of the powders at different T_a. It can be seen that there is α-Fe precipitation at 400 °C, and the precipitation is more complete at 420 °C. With the increase of annealing temperature to 440–480 °C, the grains of Fe-B start to appear. Fig. 5(c)&(d) show the powders after annealing at 420 and 480 °C for 60 min, respectively. Nanocrystalline grains are randomly distributed within the amorphous matrix. Under the annealing condition of 420 °C, the grain size is relatively small and the distribution is uniform. As shown in the inset of Fig. 5(c), the average grain size D is about 25 nm, and the diffraction rings in the SEAD image indicate the precipitation of only the α-Fe phase, corresponding to the (110), (200), and (211) planes of the α-Fe phase. As shown in Fig. 5 (d), when the annealing temperature increases to 480 °C, the amount of α-Fe precipitate gradually increases, and the grain size grows, with the grain size of about 37 nm. The diffraction rings in the SEAD image indicate the precipitation of a second phase, Fe-B, which corresponds to the XRD pattern in Fig. 5(a). The precipitation of Fe-B phase causes magnetic hardening, leading to a sharp increase in H_c. This results in higher core loss (mainly hysteresis loss) in the subsequent nano-crystalline powder cores, leading to a significant reduction in permeability and deterioration of soft magnetic properties.

The hysteresis loops measured by VSM for the annealed powders are exhibited in Fig. 6. As T_a increases from 400 to 500 °C, the B_s of the powders increases from 176.6 to 183 emu/g.

At the same time, the effects of different T_a on the properties of powder cores were studied. Fig. 7(a) shows the μ_e of $Fe_{80.5}Si_{0.5}B_{10.5}P_5Cu_{0.5}C_2Ni_1$ powder cores annealed for 60 min at different T_a. With the increase of T_a, μ_e first increases and then decreases, reaching a maximum value of 40.4 at T_a = 420 °C. With further increase in temperature, the α-Fe grain size gradually grows, and the precipitation of iron boride occurs, leading to a deterioration of the soft magnetic properties. When T_a is 400 °C, the residual internal stress is relatively high. As the temperature increases, the internal stress is more completely relieved, resulting in an initial increase in magnetic permeability. Fig. 7(b) shows the core loss P_{cv} of $Fe_{80.5}Si_{0.5}B_{10.5}P_5Cu_{0.5}C_2Ni_1$ powder cores annealed at different T_a for 60 min. The core loss of powder cores is represented

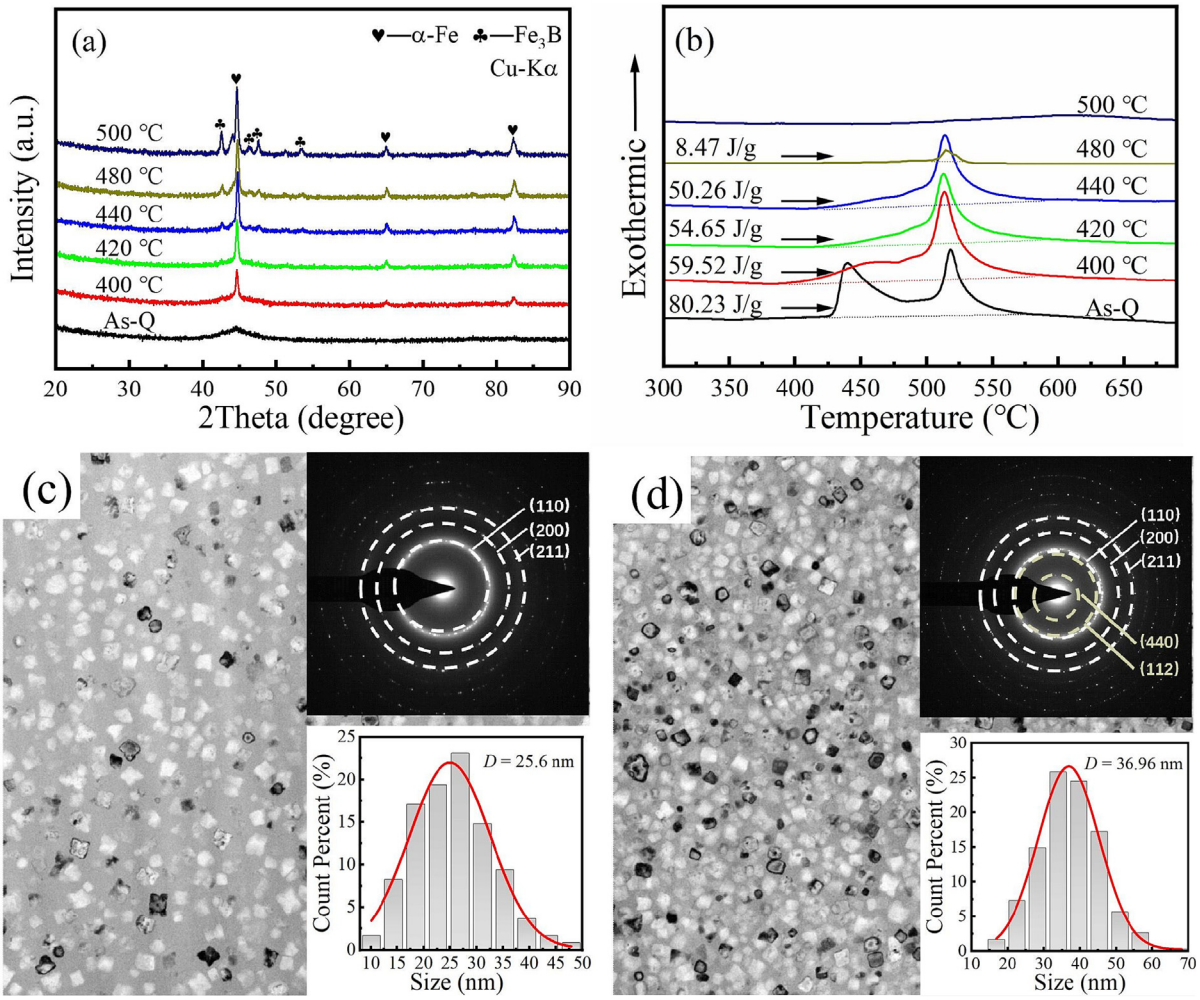

Fig. 5. (a) XRD patterns, (b) DSC curves of powders after annealing at different T_a; TEM image, SEAD image, histograms of grain size distributions of the grains of powders annealed at (c) 420 °C and (d) 480 °C.

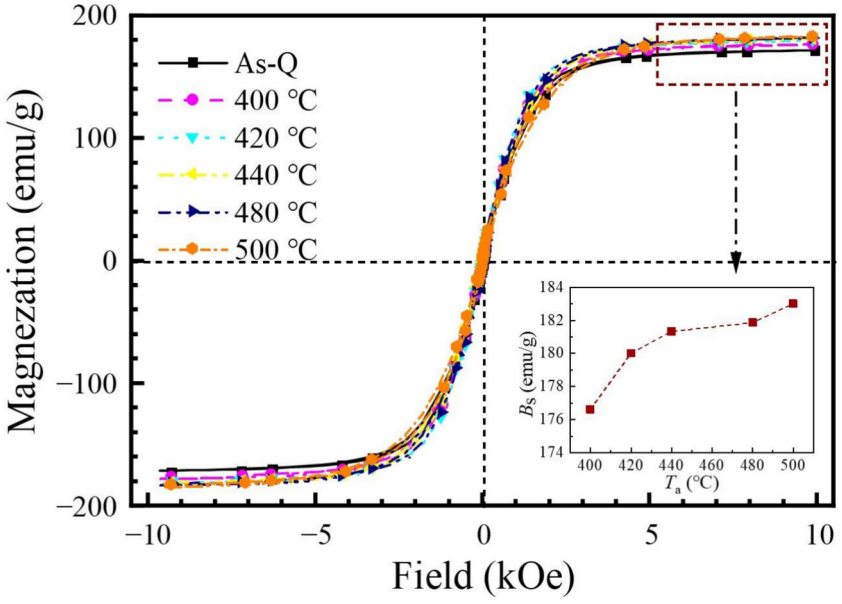

Fig. 6. Hysteresis loops of $Fe_{80.5}Si_{0.5}B_{9.5}P_5Cu_{0.5}C_2Ni_1$ powders after annealing at different T_a (The inset picture shows B_s of powders at different T_a).

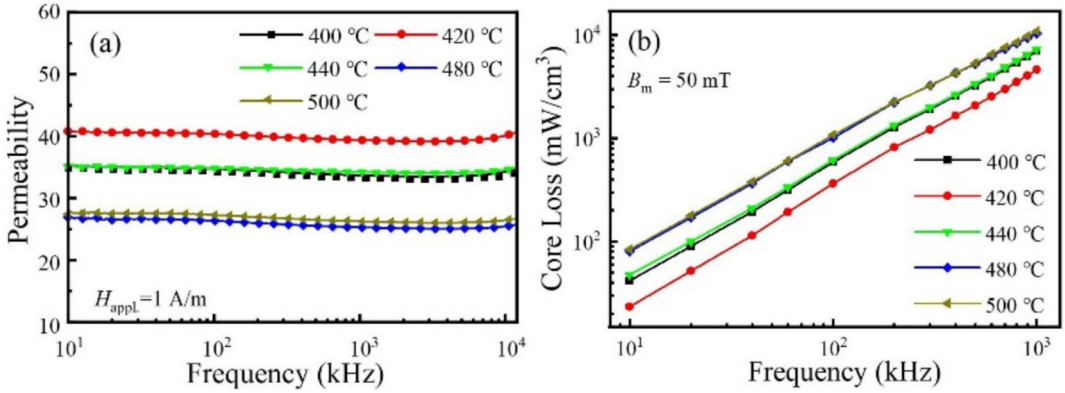

Fig. 7. (a) μ_e, (b) P_{cv} of $Fe_{80.5}Si_{0.5}B_{10.5}P_5Cu_{0.5}C_2Ni_1$ powder cores at different T_a with a B_m of 50 mT.

by equation (1), which can be divided into three components: hysteresis loss (P_h), eddy current loss (P_e), and residual loss (P_{ex}) [40]:

$$P_{cv} = P_h + P_e + P_{ex} \quad (1)$$

where all terms are typically measured in W/kg or W/m^3.

According to previous research, the value of residual loss (P_{ex}) can generally be neglected. At low frequencies, hysteresis loss dominates the core loss, which is primarily related to the microstructure of the material and the size of the powder particles. The hysteresis loss can be expressed by the following equation (2) [41]:

$$P_h = f \oint HdB \quad (2)$$

where f is the frequency in Hz, H is the magnetic field strength in A/m, and B is the magnetic flux density in T.

At high frequency condition, eddy current loss dominates, which is divided into inter particle eddy current loss (P_{inter}) and intra particle eddy current loss (P_{intra}), expressed by equation (3) [42]:

$$P_e = P_{inter} + P_{intra} = \frac{(\pi d_{eff} B_m)^2}{\beta R_{core} \rho} f^2 + \frac{(\pi d B_m)^2}{20 R_{Fe} \rho} f^2 \quad (3)$$

where ρ (kg/m^3) is the density of powder cores, B_m (T) is the maximum induction, f (Hz) is the frequency, d_{eff} (m) is the effective dimension for eddy current, R_{core} (Ω m) is the specific resistivity, β is the geometrical coefficient, d (m) is the particle diameter and R_{Fe} (Ω m) is the specific resistivity of iron.

The core loss of all powder core samples increases with increasing frequency. In contrast to the trend observed for magnetic permeability, the core loss values initially decrease and then increase with the rise in annealing temperature, reaching the lowest value at T_a = 420 °C, where $P_{cv(50mT/1MHz)} \approx 4613.8$ mW/cm^3. At this temperature, the powder core exhibits higher density, smaller gaps between particles, reduced porosity, and a decrease in hysteresis loss. However, further temperature increases lead to the precipitation of the Fe-B phase, which raises H_c and hysteresis loss. Additionally, the dissolution of the epoxy resin coating on the particle surfaces at higher temperatures reduces inter-particle resistivity, increasing eddy current loss and thereby degrading the soft magnetic properties of the powder core.

According to the above experimental results, the powder core of $Fe_{80.5}Si_{0.5}B_{10.5}P_5Cu_{0.5}C_2Ni_1$ annealed at 420 °C for 60 min exhibits excellent soft magnetic properties.

3.4. Effect of phosphoric acid passivation on the soft magnetic properties

Phosphoric acid passivation is commonly used in industry to apply an insulating coating to soft magnetic powders. In this study, phosphoric acid passivation was employed to prepare the powder cores, aiming to reduce core loss.

The magnetic properties of the powder cores passivated with different concentrations of phosphoric acid were tested, and the relationship between concentration and soft magnetic properties was established. Fig. 8(a) shows the μ_e of $Fe_{80.5}Si_{0.5}B_{10.5}P_5Cu_{0.5}C_2Ni_1$ powder cores after passivation with various concentrations. It can be seen that the μ_e decreases after passivation treatment, following passivation, which is attributed to the introduction of non-

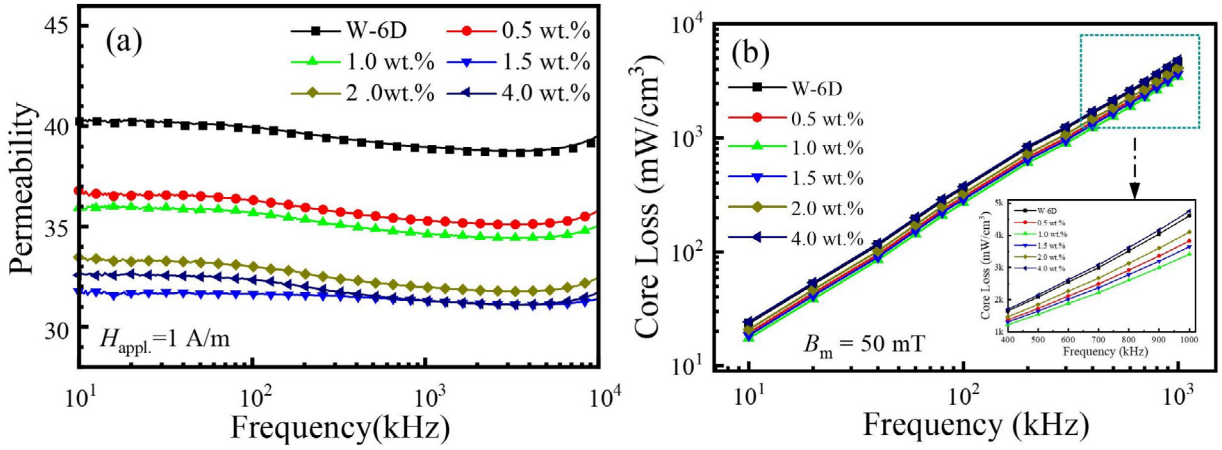

Fig. 8. (a) μ_e and (b) P_{cv} (at B_m = 50 mT) of $Fe_{80.5}Si_{0.5}B_{10.5}P_5Cu_{0.5}C_2Ni_1$ powder cores after passivation treatment with different phosphoric acid concentrations.

magnetic substances into the surface phosphate layer formed during the passivation process, leading to magnetic dilution. When the phosphoric acid concentration for passivation is 1 wt.%, the magnetic permeability decreases to 36, and further increases in concentration to 4 wt.% result in a continued decrease in μ_e to 31. Additionally, higher magnetic permeability can help reduce eddy current loss, particularly in high-frequency applications. The P_e arises from the closed current paths induced within magnetic materials, resulting in additional resistive losses and affecting material performance. In high-frequency applications, materials with high magnetic permeability and low conductivity are often preferred, or layered/coated structures are used to minimize eddy current effects.

Table 1
Density and resistivity of $Fe_{80.5}Si_{0.5}B_{10.5}P_5Cu_{0.5}C_2Ni_1$ powder cores with different phosphoric acid concentrations.

Phosphoric acid (wt.%)	Density (g/cm^3)	Resistivity $\times 10^8$(Ω·m)
0	5.58	1.47×10^{-4}
0.5	5.59	1.65
1.0	5.77	7.12
1.5	5.68	2.48
2.0	5.59	1.96
4.0	5.57	1.26

Fig. 8(b) shows the total core loss curves of the powder cores after passivation with different concentrations of phosphoric acid. It can be seen that the P_{cv} first decreases and then increases as the phosphoric acid concentration increases, reaching the lowest value at 1 wt.%, with $P_{cv(50mT/1MHz)} \approx 3414$ mW/cm^3. As mentioned in the last section, P_e can be divided into intra particle eddy current loss (P_{intra}) and inter particle eddy current loss (P_{inter}). The P_{intra} is related to the resistivity of the magnetic powder itself. And we can usually reduce the P_{inter} by evenly coating the insulating layer on the surface of the magnetic powder, thus reducing the P_e [42,43].

According to Table 1, the density of the powder core first increases and then decreases with the increase in phosphoric acid concentration. At 1 wt.%, the density reaches its maximum value of 5.7 g/cm^3, after which further increases in phosphoric acid concentration result in a gradual decrease in density. Additionally, the uniformly coated phosphate layer enhances the resistivity, as shown in Table 1. At a passivation concentration of 1 wt.%, the resistivity of the core reaches the highest value of 7.12 × 10^8

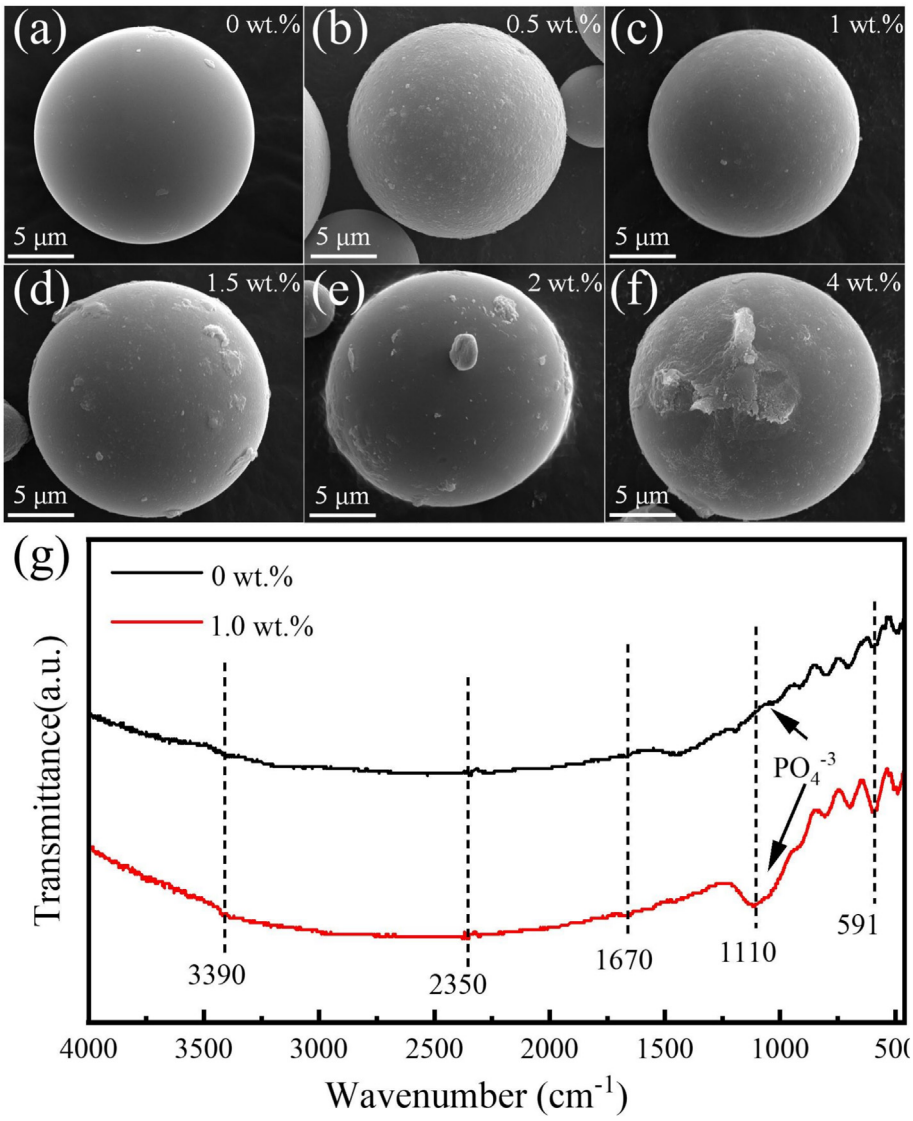

Fig. 9. (a-f) SEM images of $Fe_{80.5}Si_{0.5}B_{10.5}P_5Cu_{0.5}C_2Ni_1$ powder after phosphate passivation treatment with the phosphoric acid concentrations of 0, 0.5, 1, 1.5, 2, and 4 wt.%; (g) FTIR images of $Fe_{80.5}Si_{0.5}B_{10.5}P_5Cu_{0.5}C_2Ni_1$ powder before and after 1 wt.% phosphoric acid passivation treatment.

Ω·m, which helps reduce the P_{inter}. Therefore, an optimal phosphoric acid passivation concentration is beneficial for improving the soft magnetic properties of the powder cores.

The microscopic morphology of powders passivated with different concentrations of phosphoric acid is characterized in Fig. 9. The untreated powder in Fig. 9 (a) has a smooth surface and high sphericity. Fig. 9(b)-(f) show the surface morphology of powder particles after passivation with phosphoric acid concentration of 0.5–4 wt.%. At a phosphoric acid concentration of 0.5 wt.%, the surface begins to exhibit roughness, indicating that iron ions start reacting with dihydrogen phosphate to form a phosphate layer. As the concentration increases, the coating gradually thickens. When the concentration is 1 wt.%, the phosphate layer on the surface of the powder is compact and uniform. As the concentration increases, the coating gradually thickens. At 1 wt.%, the phosphate layer on the surface is compact and uniform. However, as the concentration continues to increase, the coating begins to clump due to excessive precipitation, and the outer layer detaches. Infrared spectroscopy can be used to characterize the functional groups and chemical bonds in the phosphate layer on the powder surfaces. The FTIR image of $Fe_{80.5}Si_{0.5}B_{10.5}P_5Cu_{0.5}C_2Ni_1$ powder after phosphoric acid passivation (0 and 1 wt.%) is shown in Fig. 9(g). The absorption peaks at 591 cm^{-1} and 1110 cm^{-1} are O-P-O bonds and P-O-Fe bonds, representing the phosphate layer on the surface of the powder and proving that the phosphate iron bond is on the surface of the ferromagnetic powder. The absorption peaks at 1670 cm^{-1} and 3390 cm^{-1} are caused by H-O–H bending, indicating that the ferromagnetic powder adsorbs H_2O molecules. However, the hydrogen bonding of OH^- and the interaction between phosphate and phosphate may lead to agglomeration, so the concentration of phosphate passivation should be appropriate. The C=O stretching occurring at 2350 cm^{-2} is due to the adsorption of CO_2 in air.

4. Conclusions

This study successfully developed a Fe-Si-B-P-Cu-C-Ni nanocrystalline alloy system with high magnetic induction. The main findings are summarized as follows:

1) The addition of a small amount of Ni (1 at.%) improves the AFA while maintaining low H_c and high B_s. The $Fe_{80.5}Si_{0.5}B_{4.5}P_{11}Cu_{0.5}C_2Ni_1$ nano-crystalline ribbons exhibit optimal soft magnetic properties with B_s = 177.5 emu/g and H_c = 3.2 A/m.
2) Increasing the B concentration enhances the AFA and expands the heat treatment temperature window in the Fe-Si-B-P-Cu-C-Ni alloy system. $Fe_{80.5}Si_{0.5}B_{10.5}P_5Cu_{0.5}C_2Ni_1$ powders with 10.5 at.% B show excellent magnetic properties ($B_s \approx$ 171.5 emu/g), with the highest B_s of 180 emu/g achieved after annealing at 420 °C.
3) Cold-pressed powder cores exhibit high permeability ($\mu_e \approx$ 40.4) and low core loss ($P_{cv(50mT/1MHz)}$ = 4613.8 mW/cm^3). Passivation with 1 wt.% phosphoric acid further reduces core loss by 26 %, bringing the P_{cv} down to 3414 mW/cm^3, while maintaining high B_s and permeability.

Future research will focus on optimizing insulation coating methods and compaction processes to further enhance the performance of these soft magnetic composites for high-frequency applications.

CRediT authorship contribution statement

Han Gao: Writing – original draft, Investigation, Data curation. **Yanan Chen:** Writing – review & editing, Methodology, Investigation, Data curation. **Bo Lin:** Methodology. **Yuanfei Cai:** Methodology, Investigation. **Xiaoying Huang:** Methodology, Investigation. **Meng Gao:** Resources, Methodology, Investigation. **Yaocen Wang:** Methodology, Investigation. **Likun Chen:** Software, Resources. **Wei Xu:** Software, Investigation. **Xing Tong:** Resources, Methodology. **Hai Guo:** Visualization, Resources. **Wenbo Wang:** Software, Resources. **Mingliang Xiang:** Writing – review & editing, Supervision, Methodology. **Jun-Qiang Wang:** Writing – review & editing, Resources, Methodology, Investigation, Funding acquisition. **Yan Zhang:** Writing – review & editing, Supervision, Funding acquisition.

Declaration of competing interest

The authors declare that they have no known competing financial interests or personal relationships that could have appeared to influence the work reported in this paper.

Acknowledgments

We acknowledge financial support from the Ningbo major R&D Plan Project (Grant No. 2025Z073), National Natural Science Foundation of China (52231006, 92163108), Zhejiang Province Key R&D Program (2022C01023), and Ningbo Yongjiang Talent Introduction Programme (2022A-011-G). This work was also partially supported by the joint project with Shenzhen Sunlord Electronics Co., Ltd. (NIMTE-51-2023-15).

References

[1] S. Lu, M. Wang, Z. Zhao, Recent advances and future developments in Fe-based amorphous soft magnetic composites, J. Non-Cryst. Solids 616 (2023) 122440.
[2] M. Persson, Advances in powder metallurgy soft magnetic composite materials for electrical machines, IEEE Colloquium on Impact of New Materials on Design (1995) 4/1-4/6.
[3] J.J. Zhong, Y.G. Guo, J.G. Zhu, Z.W. Lin, Characteristics of soft magnetic composite material under rotating magnetic fluxes, J. Magn. Magn. Mater. 299 (2006) 29–34.
[4] P. Duwez, S.C.H. Lin, Amorphous Ferromagnetic Phase in Iron-Carbon-Phosphorus Alloys, J. Appl. Phys. 38 (1967) 4096–4097.
[5] P. Sharma, X. Zhang, Y. Zhang, A. Makino, Competition driven nanocrystallization in high B_s and low coreloss Fe-Si-B-P-Cu soft magnetic alloys, Scr. Mater. 95 (2015) 3–6.
[6] H.R. Lashgari, D. Chu, S. Xie, H. Sun, M. Ferry, S. Li, Composition dependence of the microstructure and soft magnetic properties of Fe-based amorphous/nanocrystalline alloys: A review study, J. Non-Cryst. Solids 391 (2014) 61–82.
[7] L. Shi, K. Yao, Composition design for Fe-based soft magnetic amorphous and nanocrystalline alloys with high Fe content, Mater. Des. 189 (2020) 108511.
[8] T. Takahashi, K. Yoshida, Y. Shimizu, A.D. Setyawan, M. Bito, M. Abe, A. Makino, Fe-Si-B-P-C-Cu nanocrystalline soft magnetic powders with high B_s and low core loss, AIP Adv. 7 (2017) 056111.
[9] H. Yu, G. Zhang, L. Meng, X. Li, Z. Li, B. Dong, S. Zhou, Composition design of high B_s Fe-based amorphous powders with good sphericity, J. Magn. Magn. Mater. 582 (2023) 171007.
[10] Y. Zhang, P. Sharma, A. Makino, Sintered magnetic cores of high B_s $Fe_{84.3}Si_4B_8P_3Cu_{0.7}$ nano-crystalline alloy with a lamellar microstructure, J. Appl. Phys. 115 (2014) 17A322.
[11] M. Ohta, N. Chiwata, Development of Fe-based high B_s nanocrystalline alloy powder, J. Magn. Magn. Mater. 509 (2020) 166838.
[12] A. Wang, C. Zhao, A. He, H. Men, C. Chang, X. Wang, Composition design of high B_s Fe-based amorphous alloys with good amorphous-forming ability, J. Alloys Compd. 656 (2016) 729–734.
[13] J.-F. Li, X. Liu, S.-F. Zhao, H.-Y. Ding, K.-F. Yao, Fe-based bulk amorphous alloys with iron contents as high as 82 at%, J. Magn. Magn. Mater. 386 (2015) 107–110.
[14] X. Fan, T. Zhang, M. Jiang, W. Yang, B. Shen, Synthesis of novel FeSiBPCCu alloys with high amorphous forming ability and good soft magnetic properties, J. Non-Cryst. Solids 503–504 (2019) 36–43.
[15] M. Khajepour, S. Sharafi, Characterization of nanostructured Fe-Co-Si powder alloy, Powder Technol. 232 (2012) 124–133.
[16] Y.Y. Zheng, Y.G. Wang, G.T. Xia, Amorphous soft magnetic composite-cores with various orientations of the powder-flakes, J. Magn. Magn. Mater. 396 (2015) 97–101.
[17] E.Y. Kang, Y.B. Kim, K.Y. Kim, Y.H. Chung, H.K. Baik, Preparation of Fe-Si-B-Nb amorphous powder cores with excellent high-frequency magnetic properties, J. Magn. Magn. Mater. 304 (2006) e182–e185.

[18] X.-G. Li, Q. Zhu, S. Shu, J.-Z. Fan, S.-M. Zhang, Fine spherical powder production during gas atomization of pressurized melts through melt nozzles with a small inner diameter, Powder Technol. 356 (2019) 759–768.
[19] Y. Liu, Y. Yi, W. Shao, Y. Shao, Microstructure and magnetic properties of soft magnetic powder cores of amorphous and nanocrystalline alloys, J. Magn. Magn. Mater. 330 (2013) 119–133.
[20] Z. Hao, L. Wei, L. Gao, Y. Wang, X. Bai, X. Tong, X. Liang, N. Yodoshi, R. Umetsu, Y. Kawazoe, Y. Zhang, C. Cao, Effect of P addition on soft magnetic properties of Fe-Si-B-P-Cu-C nano-crystalline alloys, Intermetallics 151 (2022) 107713.
[21] A.D. Wang, H. Men, B.L. Shen, G.Q. Xie, A. Makino, A. Inoue, Effect of P on crystallization behavior and soft-magnetic properties of $Fe_{83.3}Si_4Cu_{0.7}B_{12-x}P_x$ nanocrystalline soft-magnetic alloys, Thin Solid Films 519 (2011) 8283–8286.
[22] Z. Chen, Q. Zhu, Z. Zhu, F. Chen, Q. Hu, K. Zhang, J. Hu, Y. Jiang, Effects of P addition on the glass forming ability, crystallization behaviour and soft magnetic properties of FeNi-based amorphous alloy, Intermetallics 144 (2022) 107533.
[23] Y. Li, N. Shen, Y. Wu, S. Zhang, Z. He, F. Li, X. Hui, High B_s Fe-B-P-C-Cu nanocrystalline alloy with longtime annealing stability and low heating rate sensitivity, J. Magn. Magn. Mater. 543 (2022) 168623.
[24] A. Makino, T. Kubota, K. Yubuta, A. Inoue, A. Urata, H. Matsumoto, S. Yoshida, Low core losses and magnetic properties of $Fe_{85-86}Si_{1-2}B_8P_4Cu_1$ nanocrystalline alloys with high B for power applications (invited), J. Appl. Phys. 109 (2011) 07A302.
[25] P. Sharma, X. Zhang, Y. Zhang, A. Makino, Influence of microstructure on soft magnetic properties of low coreloss and high B_s $Fe_{85}Si_2B_8P_4Cu_1$ nanocrystalline alloy, J. Appl. Phys. 115 (2014) 17A340.
[26] L. Jiang, Y. Zhang, X. Tong, T. Suzuki, A. Makino, Unique influence of heating rate on the magnetic softness of $Fe_{81.5}Si_{0.5}B_{4.5}P_{11}Cu_{0.5}C_2$ nanocrystalline alloy, J. Magn. Magn. Mater. 471 (2019) 148–152.
[27] X. Jia, Y. Li, L. Wu, W. Zhang, A study on the role of Ni content on structure and properties of Fe-Ni-Si-B-P-Cu nanocrystalline alloys, J. Alloys Compd. 822 (2020) 152784.
[28] Z. Luo, X.a. Fan, B. Feng, Z. Yang, D. Chen, S. Jiang, J. Wang, Z. Wu, X. Liu, G. Li, Y. Li, Highly enhancing electromagnetic properties in Fe-Si/MnO-SiO_2 soft magnetic composites by improving coating uniformity, Adv. Powder Technol. 32 (2021) 4846–4856.
[29] B. Zhou, Y. Dong, L. Liu, L. Chang, F. Bi, X. Wang, Enhanced soft magnetic properties of the Fe-based amorphous powder cores with novel TiO_2 insulation coating layer, J. Magn. Magn. Mater. 474 (2019) 1–8.
[30] W. Li, Z. Wang, Y. Ying, J. Yu, J. Zheng, L. Qiao, S. Che, In-situ formation of Fe_3O_4 and ZrO_2 coated Fe-based soft magnetic composites by hydrothermal method, Ceram. Int. 45 (2019) 3864–3870.
[31] Z. Chen, X. Liu, X. Kan, Z. Wang, R. Zhu, W. Yang, Q. Wu, M. Shezad, Phosphate coatings evolution study and effects of ultrasonic on soft magnetic properties of FeSiAl by aqueous phosphoric acid solution passivation, J. Alloys Compd. 783 (2019) 434–440.
[32] H.-I. Hsiang, L.-F. Fan, J.-J. Hung, Phosphoric acid addition effect on the microstructure and magnetic properties of iron-based soft magnetic composites, J. Magn. Magn. Mater. 447 (2018) 1–8.
[33] T.D. Shen, R.B. Schwarz, J.D. Thompson, Soft magnetism in mechanically alloyed nanocrystalline materials, Phys. Rev. B 72 (2005) 014431.
[34] K. Suzuki, R. Parsons, B. Zang, K. Onodera, H. Kishimoto, T. Shoji, A. Kato, Nanocrystalline soft magnetic materials from binary alloy precursors with high saturation magnetization, AIP Adv. 9 (2019) 035311.
[35] J.-F. Li, Y. Shao, X. Liu, K.-F. Yao, Fe-based bulk amorphous alloys with high glass formation ability and high saturation magnetization, Sci. Bull. 60 (2015) 396–399.
[36] Z.P. Li, R. Zang, B. Kishimoto, H. Shoji, T. Kato, A. Karel, J. Suzuki, K., Dramatic grain refinement and magnetic softening induced by Ni addition in Fe-B based nanocrystalline soft magnetic alloys, Scr. Mater. 181 (2020) 82–85.
[37] N. Aronhime, E. Zoghlin, V. Keylin, X. Jin, P. Ohodnicki, M.E. McHenry, Magnetic properties and crystallization kinetics of $(Fe_{100-x}Ni_x)_{80}Nb_4Si_2B_{14}$ metal amorphous nanocomposites, Scr. Mater. 142 (2018) 133–137.
[38] F. Shen, B. Zang, L. Song, J. Huo, Y. Zhang, J.-Q. Wang, Ultra-fine microstructure and exceptional low coercivity developed in a high-B_s Fe-Si-B-P alloy by co-alloying Ni, Mo, and Cu, Scr. Mater. 236 (2023) 115666.
[39] C. Si, Z. Zhang, Q. Zhang, J. Cai, Influence of mechanical alloying on the particle size, microstructure and soft magnetic properties of coarse Fe-based amorphous powders prepared by gas atomization, J. Non-Cryst. Solids 559 (2021) 120675.
[40] S. Flohrer, R. Schafer, J. McCord, S. Roth, L. Schultz, G. Herzer, Magnetization loss and domain refinement in nanocrystalline tape wound cores, Acta Mater. 54 (2006) 3253–3259.
[41] Y. Zhang, Y. Dong, B. Zhou, Q. Chi, L. Chang, M. Gong, J. Huang, Y. Pan, A. He, J. Li, X. Wang, Poly-para-xylylene enhanced Fe-based amorphous powder cores with improved soft magnetic properties via chemical vapor deposition, Mater. Des. 191 (2020) 108650.
[42] P. Kollár, Z. Birčáková, J. Füzer, R. Bureš, M. Fáberová, Power loss separation in Fe-based composite materials, J. Magn. Magn. Mater. 327 (2013) 146–150.
[43] H. Chen, Y. Wang, Y. Yao, J. Qu, F. Yun, Y. Li, S.P. Ringer, M. Yue, R. Zheng, Attractive-domain-wall-pinning controlled Sm-Co magnets overcome the coercivity-remanence trade-off, Acta Mater. 164 (2019) 196–206.